ELSEVIER

Materials Science and Engineering A317 (2001) 145–152

MATERIALS SCIENCE & ENGINEERING A

www.elsevier.com/locate/msea

A comparison of the mechanisms of fatigue-crack propagation behavior in a Zr-based bulk amorphous metal in air and an aqueous chloride solution

V. Schroeder [a], C.J. Gilbert [a], R.O. Ritchie [a,*]

[a] *Department of Materials Science and Engineering, University of California, Berkeley, CA 94720-1760, USA*

Abstract

Bulk amorphous alloys, such as the $Zr_{41.2}Ti_{13.8}Cu_{12.5}Ni_{10}Be_{22.5}$ (at.%) alloy, have received much interest lately, particularly for their commercial application in golf club heads. This study seeks to investigate the fatigue behavior of this Zr-based amorphous metal in the presence of air and sodium chloride solution, with the specific goal of identifying mechanisms of environmentally assisted fatigue-crack growth in these environments. Results from experiments, including fatigue testing in air and sodium chloride, fatigue under potential control, and static load testing in sodium chloride, suggest that quite distinct mechanisms of fatigue-crack propagation are active in air and sodium chloride solution. Specifically, the fatigue-crack growth rates observed under static and cyclic loading in sodium chloride likely depend on an anodic process, which results in a brittle mode of failure. Conversely in air, fatigue-crack propagation is associated with alternating blunting and re-sharpening of the crack tip, as evidenced by the presence of classic fatigue striations.

Keywords: Metallic glass; Fatigue; Stress–corrosion cracking; Failure mechanisms

1. Introduction

Since the discovery of the first metallic glass in 1960 [1], various compositions of metallic glass have been fabricated as thin ribbons or wires of less than 1 mm in thickness. Recently, however, new classes of amorphous metals with more stable amorphous phases have been developed which can be processed in bulk form. These new classes of alloys, most prominently the Zr–Ti–Cu–Ni–Be [2], Zr–Cu–Ni–Al [3], and Pd–Cu–Ni–P [4] systems, require cooling rates of less than 10 K s^{-1}, about five to six orders of magnitude slower than the rates required for early metallic glasses. Some studies on thin ribbons of metallic glass have established that amorphous metals are generally ductile [5–7]. During room temperature tests at high stresses, this ductility manifests in inhomogeneous flow that concentrates in shear bands, lying on or near planes of maximum shear [8]. Although some type of plastic flow occurs in these shear bands, the amorphous structure precludes dislocation motion. Hence, while mechanisms of plastic deformation have been proposed, such as local softening via adiabatic heating or increases in local free volume, agreement has not been reached on the active deformation mechanism in amorphous metals.

Less information is known about deformation processes responsible for fracture and fatigue in amorphous alloys. Recently, it has been determined experimentally that the $Zr_{41.2}Ti_{13.8}Cu_{12.5}Ni_{10}Be_{22.5}$ (at.%) alloy has high tensile strength ($\sim$1.9 GPa) [9] and toughness properties (K_{Ic} $\sim$18–59 MPa$\sqrt{m}$, depending upon the loading rate) [10–12]. Moreover, in air, this alloy exhibits fatigue-crack growth properties that are comparable to ductile crystalline metals [10,13].

With respect to environmentally assisted fracture, stress-corrosion cracking (SCC) experiments in aqueous solutions have been conducted on thin ribbons of amorphous metal. In these studies, iron-based amorphous metals with excellent corrosion properties exhibited SCC in acidic, chloride-containing environments [14–18]. Specifically, iron-based alloys with high concentrations of chromium showed stress–corrosion cracking behavior comparable to an unsensitized stain-

* Corresponding author.
E-mail address: roritchie@lbl.gov (R.O. Ritchie).

0921-5093/01/$ - see front matter
PII: S0921-5093(01)01157-1

less steel [18]. It was noted that fracture surfaces resulting from SCC tests had a brittle appearance [18], and that significant crack branching occurred [15]. To date, however, no SCC data exist for bulk metallic glasses.

In the present study, we compare the fatigue properties of the $Zr_{41.2}Ti_{13.8}Cu_{12.5}Ni_{10}Be_{22.5}$ amorphous metal in the presence of room air and sodium chloride solution, with the specific goal of identifying the salient mechanisms of fatigue-crack growth in each environment.

2. Experimental procedures

As-received plates of $Zr_{41.2}Ti_{13.8}Cu_{12.5}Ni_{10}Be_{22.5}$ (at%) (commercial name, Vitreloy 1) were processed by Hitchener Manufacturing Co. (Milford, NH) and provided by Amorphous Technologies International, Corp. (Laguna Niguel, CA). These plates were machined into compact-tension (C(T)) specimens with a thickness of 4.4 mm and a width of 20 mm. To insure that residual stresses present in the casting [13] did not affect behavior, $\sim$1.5 mm of material was removed from all surfaces of the casting prior to machining. Fatigue tests were conducted at room temperature ($\sim$22°C) in air (relative humidity $\sim$25–35%), in aerated de-ionized water, and in an aerated 0.5 M NaCl (98 + %, Aldrich) aqueous solution (pH $\sim$6.1) prepared with de-ionized water. Samples were loaded at a constant load ratio ($R = K_{min}/K_{max}$) of 0.1 and a frequency (ν) of 25 Hz (sine wave) on an MTS model 831 servo-hydraulic test frame; testing procedures were in general accordance with ASTM standard E647. Tests were performed under both increasing and decreasing stress–intensity control, ΔK, using a stress intensity gradient of ± 0.1 mm^{-1}. During cycling, crack lengths were monitored with unloading compliance, obtained from a back-face strain gauge. Specimens tested in both air and aqueous solution were first pre-cracked in air. The pre-crack was initiated from the notch at a ΔK of 6 $MPa\sqrt{m}$ and propagated 2 mm while ΔK decreased at a rate of -0.1 mm^{-1}. In cases where fatigue measurements were subsequently performed in an aqueous environment, solution was added while cycling the sample at ΔK of 1 $MPa\sqrt{m}$. Representative data for each environment are presented as fatigue-crack growth rates per cycle, da/dN, as a function of the applied stress–intensity range ($\Delta K = K_{max} - K_{min}$). Following fatigue experiments, a scanning electron microscope (SEM) was used to evaluate fatigue and overload fracture surfaces.

In addition to the open circuit measurements, a number of fatigue tests was also performed under potential control. During electrochemical experiments, the potential was controlled by an EG & G Model 363 potentiostat/galvanostat. Electrical connection was made to the electrodes with an aluminum alloy wire, attached to the sample with silver epoxy that was subsequently covered with electronically and ionically nonconductive Miccrostop (Tolber, Hope, AR). After adding solution to the cell containing the unloaded specimen, the potential of the C(T) specimen was maintained at -2500 mV with a saturated calomel reference electrode (SCE) and a platinum counter electrode for 5 min to reduce any air-formed oxide. After the initial polarization, crack propagation was initiated at open circuit, from the fatigue pre-crack, under sinusoidal loading conditions with $\Delta K = 1.5$ $MPa\sqrt{m}$, $R = 0.1$, and $\nu = 25$ Hz. When the crack grew by $\sim$300 μm under open circuit conditions, a potential of -600 mV was imposed and the crack-growth rate measured. The potential was subsequently stepped down to -800 mV, and back up to $+100$ or $+900$ mV in 100 mV increments. At each potential, growth rates were measured over 300–500 μm of crack growth. On two samples, the potential was held at $+900$ mV for up to 1 mm of growth, at which point the potential was stepped directly to -900 mV, while time and crack growth were monitored.

To compare with the cyclic crack-growth results, stress–corrosion cracking tests were also performed at constant load (increasing K) and at open circuit potential using C(T) specimens that were initially fatigue pre-cracked in air and finally in the test solution. Because of the relatively low driving forces needed to drive the crack, a high precision load cell was used, which had a 200 N capacity. Stress–corrosion cracking results are presented as the crack velocity, da/dt, as a function of the applied K.

3. Results

Fatigue-crack growth behavior in several environments is shown in Fig. 1, where it is apparent that growth rates in sodium chloride solution are two to three orders of magnitude larger at an equivalent stress–intensity range, ΔK, than growth rates in air. Indeed, following an incubation period during which the crack does not measurably grow under cyclic loads, fatigue-crack growth rates for the $Zr_{41.2}Ti_{13.8}Cu_{12.5}Ni_{10}Be_{22.5}$ amorphous metal in 0.5 M NaCl solution reach a pronounced plateau at $\sim 5 \times 10^{-7}$ m per cycle for ΔK values between 1 and 6 $MPa\sqrt{m}$. Moreover, the fatigue threshold, ΔK_{TH}, decreases from $\sim$1.4 $MPa\sqrt{m}$ in air to $\sim$0.8 $MPa\sqrt{m}$ in NaCl. By contrast, de-ionized water has a practically negligible effect on the fatigue behavior of the amorphous alloy compared to behavior in air (Fig. 1).

SEM fractography following fatigue tests in air and 0.5 M NaCl revealed a distinct change in fracture morphology with ΔK value and for the two environments (Fig. 2). In NaCl, for instance, over the entire

range of ΔK, fatigue fracture surfaces are microscopically smooth and optically reflective over large areas (larger than 1 mm^2 in places). These smooth areas are separated by regions that contain long ridges and small-scale cracking (Fig. 2a). At higher magnification and with the sample tilted at 60°, the step-like nature of the surface is apparent (Fig. 2b). After fatigue in air, features similar to those described above are observed at stress intensities near ΔK_{TH}, specifically below 2.5–3 MPa$\sqrt{m}$. At higher ΔK in air, however, the surfaces are much rougher (Fig. 2c). In particular, periodic ridges (Fig. 2d) are observed with wavelengths that increase weakly with stress intensity; these ridges, possibly striations, appear in discontinuous regions of variable size on the fatigue fracture surface, and are approximately perpendicular to the direction of crack propagation. Likewise, fatigue fracture surfaces from specimens tested in de-ionized water are similar in appearance to those tested in air, over approximately the same range of ΔK values.

Tests were also performed in sodium chloride solution under static (non-cyclic) loading conditions in order to examine the severity of stress–corrosion cracking (SCC) and its role in the cyclic fatigue process. From the dependence of crack velocities on applied K (Fig. 3), it is apparent that just above the K_{ISCC} threshold (average $K_{ISCC} \sim 0.8$ MPa$\sqrt{m}$), crack velocities are essentially independent of applied K with a plateau in growth rates between 10^{-5} and 10^{-4} m s^{-1}. Moreover, incubation times, which depended on K, were also observed during SCC.

To further isolate the fatigue-crack propagation mechanism in sodium chloride solution, the amorphous

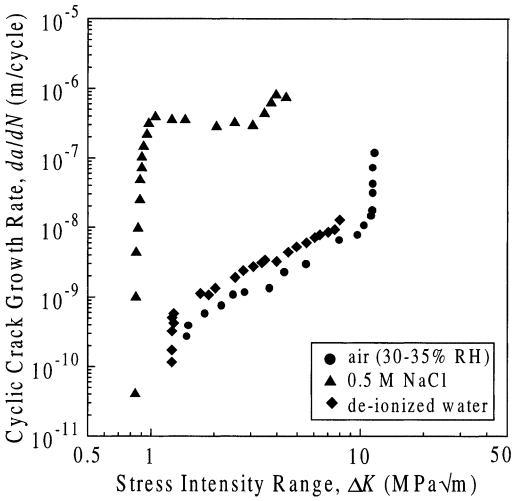

Fig. 1. Fatigue-crack growth rates (under sinusoidal loading) in amorphous $Zr_{41.2}Ti_{13.8}Cu_{12.5}Ni_{10}Be_{22.5}$ (at.%) are plotted as a function of the stress–intensity range for three environments: 0.5 M NaCl, de-ionized water, and laboratory air (relative humidity ~25–35%). The plotted data points for each condition are the result of experiments on several samples.

metal was polarized to potentials between −900 mV (SCE) and +900 mV (SCE) during cyclic fatigue tests. In Fig. 4, fatigue-crack growth rates are plotted as a function of potential for a constant ΔK of 1.5 MPa$\sqrt{m}$, where it is observed that crack-growth rates decrease rapidly from a high of $\sim 10^{-6}$–10^{-7} m per cycle as the specimen is polarized cathodically below −750 mV (SCE). Although the potential was stepped during the continuous growth of a fatigue crack, fatigue-crack growth rates stabilized in less than 100 μm of growth after each 100 mV step.

To establish the time required to arrest a fatigue crack by imposing a potential, the potential was stepped directly from +900 to −900 mV (SCE). At −900 mV, the crack arrested after 300 s and 200 μm of growth, and the growth rates began to decrease immediately (Fig. 5).

4. Discussion

The present study clearly demonstrates that the fatigue behavior of the amorphous $Zr_{41.2}Ti_{13.8}Cu_{12.5}Ni_{10}Be_{22.5}$ alloy differs significantly in air and sodium chloride solution. In sodium chloride solution, the metallic glass exhibits high fatigue-crack growth rates at low stress intensities, growth rates that do not vary with stress intensity but depend on potential, and fracture surfaces with brittle features. In air on the other hand, fatigue-crack growth rates are several orders of magnitude lower, they vary with stress intensity, and fracture surfaces have predominantly ductile features. In the following discussion, these experimentally observed differences in fatigue behavior are rationalized in terms of differences in the salient mechanisms of fatigue-crack propagation in the two environments.

4.1. Fatigue-crack propagation mechanism in air

In air, over a broad range of stress intensities, the dependence of crack-growth rates on ΔK may be characterized by the Paris power-law equation. Specifically, the fatigue data, presented in Fig. 1, may be regression fit to a power law [19] of the form, $da/dN = C\Delta K^m$, where C and m are constants. For the representative fatigue curve in air, a best fit is obtained with $C \sim 2.3 \times 10^{-10}$ and $m \sim 1.6$ (units: MPa$\sqrt{m}$ m cycle^{-1}). With respect to ΔK_{TH} and the exponent, m, the fatigue behavior of amorphous $Zr_{41.2}Ti_{13.8}Cu_{12.5}Ni_{10}Be_{22.5}$ is similar to ductile crystalline metals, such as high strength steels [20] and age-hardened aluminum alloys [21], as reported previously [13]. With respect to the fatigue-fracture instability, however, the amorphous alloy has a significantly lower value, $K_{max} \sim 13$ MPa$\sqrt{m}$, than these traditional alloys at this loading rate.

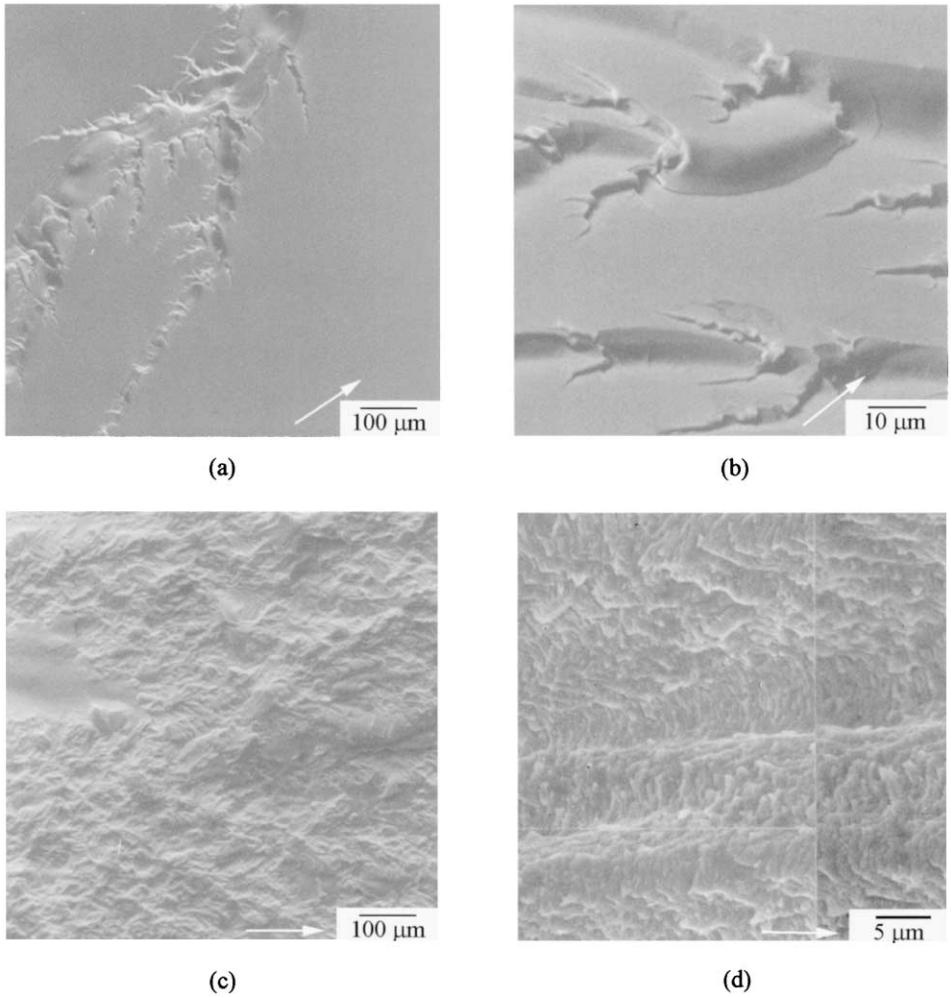

Fig. 2. Scanning electron microscopy of fatigue fracture surfaces in NaCl at $\Delta K \sim 1.5$ MPa$\sqrt{\text{m}}$ at (a) low magnification and (b) tilted 60° at higher magnification and in air at (c) low magnification at $\Delta K \sim 7$ MPa$\sqrt{\text{m}}$ and (d) at higher magnification at $\Delta K \sim 10$ MPa$\sqrt{\text{m}}$.

In addition to having Paris power-law behavior that is similar to the behavior of ductile crystalline metals, the amorphous metal exhibits striations that are frequently observed on fatigue fracture surfaces in crystalline metals [13]. Stereo-imaging of fatigue fracture surfaces clearly indicates such striations. Specifically, peaks on one fracture surface align with valleys on the other fracture surface, suggesting shearing of the metal during fatigue-crack growth [22]. Typically in these metals, the presence of striations suggests a mechanism of fatigue-crack propagation that requires plastic flow alternately to blunt and sharpen the crack tip during the loading cycle. Measured striation spacings, shown in Fig. 6, overestimate the macroscopic fatigue-crack growth rate, similar to the behavior in ductile crystalline metals. In crystalline metals, this overestimate is generally explained by the fact that the crack does not propagate uniformly over the entire crack front.

In metallic glass, such alternating blunting and resharpening presumably occurs by limited shear band formation at the crack tip, although the precise mechanism is still unclear. Shear bands have not been observed on the surface of these bulk C(T) specimens during fatigue testing. However, images acquired at the tip of fatigue cracks propagating in thin ribbons of metallic glass exhibit visible shear bands [23]. Nevertheless, using the crack-tip opening displacement, $\Delta\delta$, as a physical measure of fatigue-crack growth rates provides a good fit to the experimental data (Fig. 6):

$$\Delta\delta = \beta \frac{\Delta K^2}{\sigma_Y E'}, \tag{1}$$

where σ_Y is the flow stress ($\sigma_Y \sim 1900$ MPa), E' is E, Young's modulus, in plane stress and E' is $E/(1-\nu^2)$ in plane strain ($E \sim 90$ GPa), ν is Poisson's ratio ($\nu \sim 0.3$), and β is a scaling constant, which is a function of the efficiency of blunting and the degree of shear reversibility at the crack tip (0.01–0.1 for mode I growth) [13]; for the current data set, $\beta \sim 0.03$.

4.2. Fatigue-crack propagation mechanism in sodium chloride

As described above, the fatigue-crack growth behavior of the amorphous $Zr_{41.2}Ti_{13.8}Cu_{12.5}Ni_{10}Be_{22.5}$ alloy in air was evaluated using the Paris-power law, striation spacing and the crack-tip opening displacement relationship. In sodium chloride however, fatigue-crack growth rates are essentially independent of stress intensity, and striations are not observed on the fatigue fracture surfaces. Although the exponent m in the Paris power-law [19], $da/dN = C\Delta K^m$, is approximately 1.6 in air, it approaches zero in the plateau region of crack growth in NaCl. This plateau, which is typical of stress–corrosion fatigue, occurs at a fatigue-crack growth rate, da/dN, of about 4×10^{-7} m per cycle (equivalent to a crack velocity of $\sim 10^{-5}$ m s^{-1}).

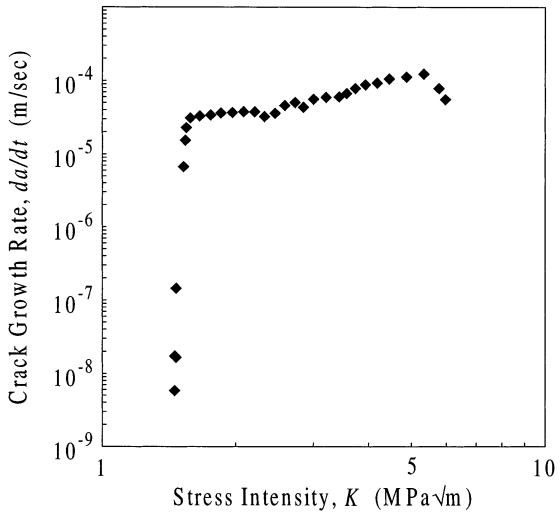

Fig. 3. Stress–corrosion cracking velocity in the amorphous $Zr_{41.2}Ti_{13.8}Cu_{12.5}Ni_{10}Be_{22.5}$ (at.%) metal under sustained load, are plotted as a function of the stress intensity, K, in aerated 0.5 M NaCl. Data shown have been acquired from one sample.

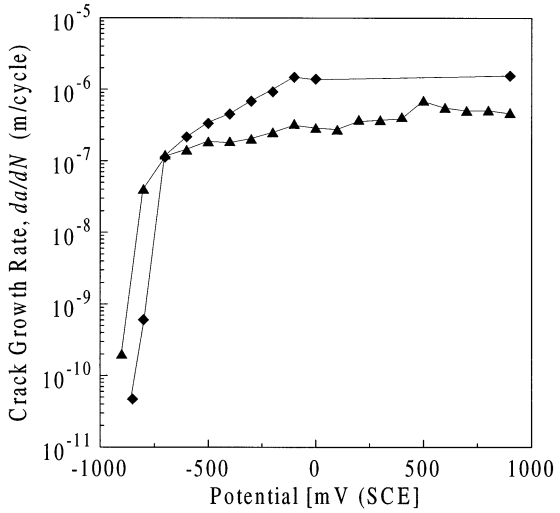

Fig. 4. Fatigue-crack growth rates at constant $\Delta K = 1.5$ MPa$\sqrt{\text{m}}$ in the amorphous $Zr_{41.2}Ti_{13.8}Cu_{12.5}Ni_{10}Be_{22.5}$ (at.%) alloy in 0.5 M NaCl, recorded during 300–500 μm of crack growth at each potential in two separate tests.

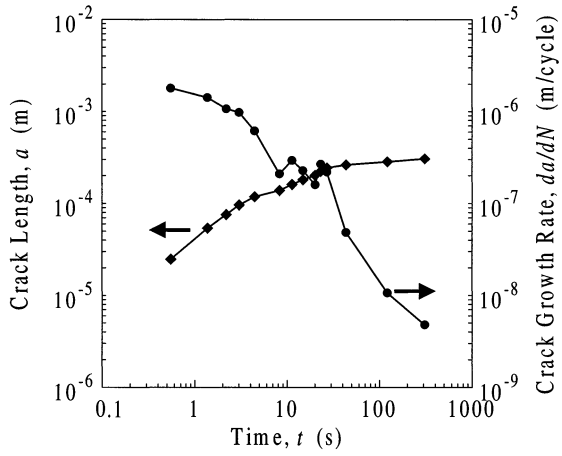

Fig. 5. Crack length and crack-growth rate at constant $\Delta K = 1.5$ MPa$\sqrt{\text{m}}$ are plotted during fatigue of amorphous $Zr_{41.2}Ti_{13.8}Cu_{12.5}Ni_{10}Be_{22.5}$ (at.%) in aerated 0.5 M NaCl after stepping from a potentiostatic hold at $+900$ mV to a hold at -900 mV (SCE).

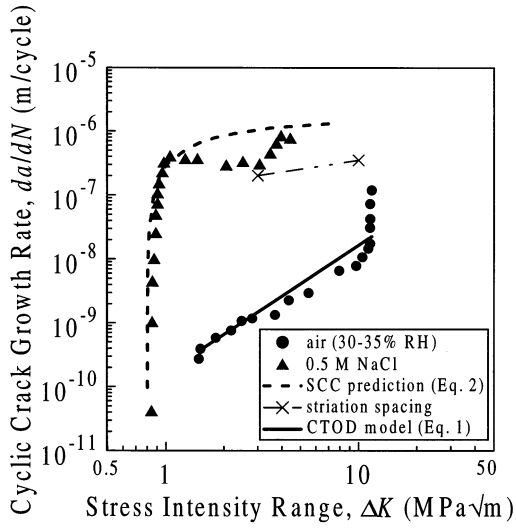

Fig. 6. Fatigue-crack growth rates (under sinusoidal loading) in amorphous $Zr_{41.2}Ti_{13.8}Cu_{12.5}Ni_{10}Be_{22.5}$ (at.%) are plotted as a function of stress–intensity range for three environments: 0.5 M NaCl, de-ionized water, and laboratory air (relative humidity $\sim$25–35%). In addition, a comparison of experimentally measured fatigue crack growth rates in NaCl to growth rates predicted by the superposition or process-competition model is shown.

Corresponding stress–corrosion fatigue experiments have not been conducted on the crystalline version of this Zr-based metal because the fracture toughness in air of the crystalline version is prohibitively low (K_{IC} ~ 1 MPa$\sqrt{\text{m}}$) for fatigue or SCC experiments [10].

In NaCl at open circuit, experimentally measured crack velocities, acquired during stress–corrosion

cracking (SCC) tests, may be used to evaluate the effect of static load on fatigue-crack growth, using superposition [24] or process-competition [25,26] models. In the superposition model, the mechanical (da/dN vs. ΔK, in a reference environment) and environmental (da/dt vs. K from stress–corrosion testing) contributions to cracking are additive, in order to predict the fatigue-crack growth rates in NaCl. In the process-competition model, on the other hand, the crack is assumed to grow at a given stress intensity by the faster of the mechanical or the environmentally-assisted mechanisms. In this case, the terms in the superposition model, aside from the SCC term, increased the predicted values of fatigue-crack growth rates in NaCl by less than 0.1%, thereby indicating that the environmental effect from static loading is the dominant contribution to fatigue-crack growth in NaCl. Thus from both models, predictions of fatigue-crack growth rates in NaCl solution have been calculated with the following relation, which integrates crack velocities, $(da/dt(K(t)))_{SCC}$, measured experimentally during SCC, over the time, t, of one fatigue cycle (Fig. 6):

$$\left(\frac{da}{dN}\right)_{eff} = \int_0^{1/\nu} \left(\frac{da}{dt}(K(t))\right)_{SCC} dt, \quad (2)$$

The model predictions, which use an average value for the onset of SCC, K_{ISCC}, of 0.8 $MPa\sqrt{m}$, are fully consistent with experimentally measured fatigue-crack growth results in NaCl (Fig. 6).

Although at open circuit, immersion in sodium chloride solution leads to high fatigue-crack growth rates (Fig. 1), cathodic polarization has been shown to reduce or eliminate this acceleration of growth rates (Fig. 4). At open circuit, the oxide film on amorphous $Zr_{41.2}Ti_{13.8}Cu_{12.5}Ni_{10}Be_{22.5}$ presumably provides limited protection because the corrosion potential (~ -200 mV) is quite close to the pitting potential (~ 0 mV) in 0.5 M NaCl [27]. In fact the corrosion potential lies between the pitting potential and the protection potential, the potential at which active pits stop growing [28]; this range of potential is linked to a high incidence of SCC in crystalline metals. Indeed, cathodically polarizing the fatigue specimen away from the pitting potential to -900 mV arrests the fatigue crack (Fig. 5). This strong effect of cathodic polarization suggests that the mechanism of fatigue-crack propagation in NaCl depends on an anodic reaction at the crack tip. This anodic reaction most likely consists of metal atoms oxidizing to their thermodynamically stable ions.

Evidently, cathodic polarization stops crack propagation that is aided by an anodic process. It is also notable that at a potential sufficiently cathodic to stop the anodic process, ~ -900 mV, a cathodic process of corrosion fatigue is not initiated. Upon cathodic polarization, a cathodic mechanism, such as hydrogen embrittlement, may be activated [29] because cathodic polarization increases the amount of hydrogen generated in reduction reactions on the bulk C(T) specimen. However, the results presented in Figs. 4 and 5 show that a cathodic process, such as hydrogen embrittlement, is not activated at -900 mV (SCE). Thus, in practice cathodic protection could be used to stop SCC in the $Zr_{41.2}Ti_{13.8}Cu_{12.5}Ni_{10}Be_{22.5}$ amorphous metal. Moreover, Fig. 5 shows that cathodic protection by potential control quickly stops crack growth in less than 200 μm.

While cathodic polarization can eliminate high growth rates in sodium chloride solution, anodic polarization has a negligible effect. The accelerated fatigue-crack growth rates do not decrease at potentials well above the pitting potential (Fig. 4). (Although the potential at the crack tip is probably not the same as the applied potential due in part to concentration gradients, the crack tip potential lies between the corrosion potential and the applied potential [30].) Typically, crystalline metals are highly susceptible to SCC at potentials just cathodic of the pitting potential, but in this case the range of susceptibility extends anodically well beyond the pitting potential.

Since the fatigue-crack growth rates are relatively independent of potential above the pitting potential, ~ 0 mV, either the active process at the crack tip is relatively independent of potential, or there are competing processes at the crack tip that separately act to accelerate and decelerate crack growth. If an anodic reaction is responsible for the high growth rates, then a Tafel-type dependence on overpotential is expected unless, for instance, a limiting current is reached above a specific potential due to mass transport limitations. Possibly, a limiting current could also limit the amount of general dissolution at the crack tip, which, if unchecked, could lead to blunting and crack arrest at anodic potentials.

Although fatigue fracture surfaces in the amorphous alloy are obviously not intergranular, SEM micrographs acquired in NaCl at all ΔK levels provide evidence of brittle-like fatigue fracture (Fig. 2a and b are representative). The fracture occurs on parallel planes approximately perpendicular to the applied load (i.e. planes of maximum normal stress); these planes have little or no shear stress, the stress normally responsible for plastic deformation. After fracture, these planes are smooth and are connected by steps on the fracture surface (Fig. 2a), which are accompanied by local cracking out of the primary planes of fracture (Fig. 2b). Steps that join planes of fracture together are also observed in cleavage fracture in ductile crystalline metals; however, in the case of cleavage fracture, evidence of plasticity is generally observed along the cleavage planes and at the steps that join the planes.

Presumably, in the case of the metallic glass, the brittle-like fracture mode is assisted by the aqueous solution, possibly chloride ions, allowing for significantly higher growth rates in 0.5 M NaCl than in air at near-threshold stress intensity even though the fracture surfaces look similar. In summary, this appears to be an example of stress–corrosion cracking and corrosion fatigue that does not rely on intergranular or transgranular fracture, although it does appear to be a brittle mode of failure.

This study demonstrates that a crystalline structure is not a prerequisite for environmentally enhanced fatigue in metals. In crystalline metals, stress–corrosion cracking (e.g. [31]) and corrosion fatigue (e.g. [32]) fracture surfaces often exhibit intergranular features at low stress–intensity ranges. An increased susceptibility to intergranular SCC has been correlated to an increased susceptibility to grain-boundary corrosion [33,34], although exceptions exist. Moreover, the increased susceptibility to intergranular corrosion has been related to the depletion of protective elements in the grain-boundary region, which weakens the oxide film [35]. This study clearly demonstrates that even in the absence of any crystal structure, and with nominally homogeneous composition, environmentally assisted low stress–intensity SCC and fatigue-crack growth occurs, producing brittle-like fracture and high crack velocities.

4.3. Comparison to studies of SCC in thin ribbons of metallic glass

For the purpose of establishing general trends in the SCC behavior of amorphous metals, results from the current study can be compared to earlier SCC studies on thin ribbon amorphous metals. In a thin ribbon of amorphous Fe–Cr–Ni–W, Jones and Wang observed brittle-like SCC fracture surfaces following a bend test in boiling $MgCl_2$, which was attributed to fast fracture following Cl^--assisted initiation [18]. However, in the current work, crack growth during SCC and fatigue of amorphous $Zr_{41.2}Ti_{13.8}Cu_{12.5}Ni_{10}Be_{22.5}$ in NaCl was fast, but stable, suggesting that the aqueous solution assisted the SCC cracking process throughout fracture and fatigue. Furthermore, heavily branched cracking, which was reported for SCC of thin ribbons of Fe–Ni–(P,B) in HCl and $FeCl_3$ [15,36], was not observed. In fact, for SCC and fatigue tests in NaCl, cracks typically propagated with no branching on a plane approximately normal to the direction of applied stress. However, in air, some branching and bridging of the crack was observed at near-threshold levels of ΔK; even in these cases a single dominant crack continued to propagate, leaving short branches and bridges in its wake.

5. Conclusions

The active mechanisms of fatigue-crack propagation in a Zr–Ti–Cu–Ni–Be amorphous alloy differ dramatically in room air and in sodium chloride solution. In air over a wide range of stress–intensity values, substantial plastic flow occurs at the crack tip; indeed, striations are observed, suggesting cyclic blunting and resharpening occurs at the crack tip such that the growth-rate data can be rationalized in terms of a crack tip opening displacement model. At low stress intensities, near the threshold stress intensity in air, the fracture surfaces appear smooth over large areas with some brittle features. Similar brittle features are observed in SEM micrographs of fatigue-fracture surfaces created in NaCl over the full range of stress intensities tested. It appears that chloride ions assist the apparently brittle fracture mechanism, generating exceptionally high growth rates, as much as three orders of magnitude higher than in air. Furthermore, the chloride-assisted mechanism dominates both static and cyclic sub-critical crack growth behavior; integration of the static data over loading cycles completely accounts for the cyclic-fatigue growth rates.

Acknowledgements

This work was supported by Howmet Corporation, with additional funding from Amorphous Technologies International and the U.S. Air Force Office of Scientific Research under Grant No. F49620-98-1-0260.

References

[1] W. Klement, R.H. Willens, P. Duwez, Nature 187 (1960) 869.
[2] A. Peker, W.L. Johnson, Appl. Phys. Lett. 63 (1993) 2342.
[3] A. Inoue, T. Zhang, N. Nishiyama, K. Ohba, T. Masumoto, Mater. Trans. JIM 34 (1993) 1234.
[4] Y. He, R.B. Schwarz, J.I. Archuleta, Appl. Phys. Lett. 69 (1996) 1861.
[5] J.J. Gilman, J. Appl. Phys. 46 (1975) 1625.
[6] A.S. Argon, Acta Metall. 27 (1979) 47.
[7] J. Megusar, A.S. Argon, N.J. Grant, in: B.H. Kear, B.C. Giessen, M. Cohen (Eds.), Rapidly Solidified Amorphous and Crystalline Alloys: Proceedings of the Materials Research Society Annual Meeting, November 1981, Elsevier Science Publishing Co., New York, 1982, p. 283.
[8] C.T. Liu, L. Heatherly, D.S. Easton, C.A. Carmichael, J.H. Schneibel, C.H. Chen, J.L. Wright, M.H. Yoo, J.A. Horton, A. Inoue, Metall. Mater. Trans. 29A (1998) 1811.
[9] H.A. Bruck, T. Christman, A.J. Rosakis, W.L. Johnson, Scripta Metall. Mater. 30 (1994) 429.
[10] C.J. Gilbert, R.O. Ritchie, W.L. Johnson, Appl. Phys. Lett. 71 (1997) 476.
[11] R.D. Conner, A.J. Rosakis, W.L. Johnson, D.M. Owen, Scripta Mater. 37 (1997) 1373.

[12] P. Lowhaphandu, J.J. Lewandowski, Scripta Mater. 38 (1998) 1811.
[13] C.J. Gilbert, V. Schroeder, R.O. Ritchie, Metall. Mater. Trans. 30A (1999) 1739.
[14] A. Kawashima, K. Hashimoto, T.T. Masumoto, Corros. Sci. 16 (1976) 935.
[15] M.D. Archer, R.J. McKim, Corrosion 39 (1983) 91.
[16] R.F. Sandenbergh, R.M. Latanision, Corrosion 41 (1985) 369.
[17] K. Habib, Scripta Metall. Mater. 31 (1994) 1669.
[18] R.H. Jones, R. Wang, Corrosion 42 (1986) 504.
[19] P.C. Paris, F. Erdogan, J. Basic Eng. 85 (1963) 528.
[20] R.O. Ritchie, J. Eng. Mater. Tech. Trans. ASME Series H 99 (1977) 195.
[21] K.T.V. Rao, W. Yu, R.O. Ritchie, Metall. Trans. 9A (1988) 549.
[22] A. Tatschl, C.J. Gilbert, V. Schroeder, R. Pippan, R.O. Ritchie, J. Mater. Res. 15 (2000) 898.
[23] T. Ogura, K. Fukushima, T. Masumoto, Scripta Metall. 9 (1975) 979–983.
[24] R.P. Wei, J.D. Landes, Mater. Res. Stand. 9 (1969) 25.
[25] I.M. Austen, E.F. Walker in International Conference on the Influence of Environment on Fatigue, (London: IMechE, 1977) 1.
[26] I.M. Austen, P. McIntyre, Metal. Sci. 13 (1979) 420.
[27] V. Schroeder, C.J. Gilbert, R.O. Ritchie, Scritpa Mater. 38 (1998) 1481.
[28] V. Schroeder, Ph.D. thesis (advisor: R.O. Ritchie), University of California, Berkeley, May 2000.
[29] A. Turnbull, Scripta Metall. 20 (1986) 365.
[30] A. Turnbull, A.S. Dolphin, F.A. Rackley, Corrosion 44 (1988) 55.
[31] C.D. Beachem, Metall. Trans. 3 (1972) 437.
[32] G. Herbsleb, W. Schwenk, Corrosion 41 (1985) 431.
[33] A. Garner, D. Tromans, Corrosion 35 (1979) 55.
[34] G.S. Was, V.B. Rajan, Metall. Trans. 18A (1987) 1313.
[35] A. Joshi, D.F. Stein, Corrosion 28 (1972) 321.
[36] M.D. Archer, R.J. McKim, J. Mater. Sci. 18 (1983) 1125.